Nanoscale

PAPER

View Article Online
View Journal | View Issue

Cite this: *Nanoscale*, 2023, **15**, 2756

The bio-inspired heterogeneous single-cluster catalyst Ni100–Fe_4S_4 for enhanced electrochemical CO_2 reduction to CH_4†

Hengyue Xu, [a] Daqin Guan [c] and Lan Ma *[a,b]

Electrochemical conversion of CO_2-to-CH_4 is a process of converting the inert greenhouse gas into energy molecules. It offers great promise for the transformation of carbon-neutral economy. However, achieving high CH_4 activity and selectivity remains a major challenge because the electrochemical reduction of CO_2-to-CH_4 is accompanied by various C_1 intermediates at the catalytic site, involving multiple proton-coupled electron transfer processes. Herein, different from the traditional designing strategy, we propose a bio-inspired theoretical design approach to construct a heterogeneous single-cluster catalyst Ni100–Fe_4S_4 at the atomic level, which may show high CO_2 electroreduction performance. Combined with the crystallographic data and theoretical calculations, Ni100–Fe_4S_4 and CO dehydrogenase exhibit highly similar catalytic geometric active centers and CO_2 binding modes. By exploring the origin of the catalytic activity of this biomimetic structure, we found that the activation of CO_2 on Ni100–Fe_4S_4 theoretically exceeds that on natural CO dehydrogenase. Density functional theory calculations reveal that the dehydrogenase enzyme-liked Fe–Ni active site serves as an electron enrichment 'electro-bridge' (an electron-rich highly active catalytic site), which can activate CO_2 molecules efficiently and stabilize various intermediates in multistep elementary reactions to selectively produce CH_4 at a low overpotential (0.13 eV). The calculated CO_2 electroreduction pathways are well consistent with the nickel-based catalytic materials reported in experimental studies. Our work showcases and highlights the rational design of high-performance catalytic materials *via* the biomimetic methodology at the atomic level.

Received 29th November 2022,
Accepted 26th December 2022

DOI: 10.1039/d2nr06665c

rsc.li/nanoscale

1. Introduction

The global energy environmental crisis is particularly prominent in the 21st century. The excessive consumption of fossil fuels has not only brought about the energy crisis, but also caused global warming,[1] water pollution,[2] extreme climate change,[3] and extinction of biological populations[4] due to excessive CO_2 emissions. Developing a carbon-neutral strategy provides breakthrough solutions to the global crisis including energy, food, and climate change. Electrochemical CO_2 reduction (CO_2RR) to useful fuels and value-added chemical feedstocks offers promising pathways for carbon neutrality. However, the rational design of low-cost, efficient, high-selectivity CO_2 electrocatalysts remains a great challenge.[5,6] Currently, the two main strategies for the design of highly active CO_2RR electrocatalysts are to increase the number of active sites on a given electrode and increase the intrinsic activity of each active site.[7] They may have transport problems and consume more expensive materials upon increasing the number of active sites on a given electrode.[7] In addition, compared with the former strategy, the latter strategy improves from key origins of catalyst activity. However, significant challenges remain in increasing the intrinsic activity of each active site, which requires a dynamic understanding of the atomic structure of the catalyst at the electronic structure level.[5] For example, Li *et al.* cleverly designed a metal–organic framework based bimetallic site catalyst with self-adaptive characteristics,[8] which achieved selective CO_2 photoreduction to CH_4. Zhang *et al.* designed a carbon nanotube-based nickel phthalocyanine catalyst at the molecular level, achieving selective CO_2 reduction.[9] Wang *et al.* designed a Ni–N–C complex catalyst from the electronic structure level by combining theoretical calculation and experiment, achieving efficient CO_2RR.[10] The electronic structure of the catalyst surface can also be adjusted

[a]*Institute of Biopharmaceutical and Health Engineering, Tsinghua Shenzhen International Graduate School, Tsinghua University, Shenzhen 518055, China. E-mail: malan@sz.tsinghua.edu.cn*
[b]*Institute of Biomedical Health Technology and Engineering, Shenzhen Bay Laboratory, Shenzhen 518055, China*
[c]*Department of Building and Real Estate, The Hong Kong Polytechnic University, Hung Hom, Kowloon 999077, Hong Kong, China*
† Electronic supplementary information (ESI) available. See DOI: https://doi.org/10.1039/d2nr06665c

through surface modification, such as tailoring on the surface of copper-based catalysts for C–C coupling[11] and the etching strategy of metal–organic framework materials.[12] At the same time, the addition of artificial intelligence provides more ideas for catalyst design. Zhong and Tran *et al.* combined active machine learning with DFT calculations to develop a catalyst computational design framework.[13,14] They further performed approximately 4000 DFT simulations, which combined with experimental testing finally revealed Cu–Al materials with highly efficient CO_2-selective reduction properties.[14] Therefore, the current design of excellent CO_2RR catalysts is extremely challenging, requiring expensive high-throughput calculations, as well as a deep understanding of the microscopic geometry and electronic structure of materials.[5,6] In other words, bionics has been gradually applied to the design of various catalysts in recent years.[15–20] From the perspective of Shafaat *et al.*, it is highly successful to design efficient CO_2 reduction catalysts by combining biological and chemical strategies.[15] It is fascinating and highly promising to propose a strategy for the bio-inspired design approach of CO_2RR catalysts at the atomic level.

The biological redox conversion of CO_2, N_2, O_2 and H_2 is an important process in biogeochemical cycles. Abundant evidence suggests that both the existence of the current biosphere and the origin of the earliest life on the Earth rely on the biological capacity to fix CO_2 and convert into living matter.[21,22] To date, seven carbon fixation pathways in nature have been discovered. As the workhorses of large-scale CO_2 fixation in nature, the Calvin cycle[23] combined with photosynthesis was first recognized in 1948, followed by the reverse Krebs cycle[24] (reverse TCA cycle) in 1966, the reductive acetyl-CoA pathway[25] (Wood–Ljungdahl pathway) in 1972, the 3-hydroxypropionate bicycle[26] (3-HP/malyl-CoA cycle) in 1993, the dicarboxylate/4-hydroxybutyrate cycle[27] in 2007 (Di-4HB cycle), the 3-hydroxypropionate-4-hydroxybutyrate cycle[28] in 2008 (3HP-4HB cycle), and the enoyl-CoA carboxylases/reductases[29] in 2016. Among these CO_2 fixation pathways in nature, the acetyl-CoA (Wood–Ljungdahl pathway) pathway is the most ancient and relies on metalloenzymes containing transition metal active centers for CO_2 activation.[30] This kind of ancient metalloenzyme is named Carbon monoxide dehydrogenase/acetyl-CoA synthase (CODHase/ACS). It may be the earliest biological carbon-fixing enzyme evolved by natural thermophilic anaerobic microorganisms in the autotrophic theory of the origin of life,[31–33] endowing it with the ability to live in the CO_2-rich atmosphere that existed during the Archean Eon.[34,35]

CO dehydrogenase has been proven to exhibit very good biological activity in CO_2 reduction.[15,36–38] Herein, inspired by the crystal structure of CO dehydrogenase II[39] isolated from *Carboxyothermus hydrogenoformans* ($CODHII_{Ch}$), we designed a heterogeneous Fe_4S_4 single-cluster catalyst on the Ni (100) face (Ni100–Fe_4S_4) for the electrocatalytic reduction of CO_2. Compared with gaseous CO_2 and adsorbed CO_2 in $CODHII_{Ch}$ from crystallographic analysis measured in experimental studies,[39,40] the adsorbed CO_2 on Ni100–Fe_4S_4 exhibits longer bond lengths and smaller bond angles, which endows Ni100–Fe_4S_4 with better CO_2 activation. Furthermore, charge difference and density of states (DOS) analyses indicated that the electrons of Ni atoms and the Fe_4S_4 iron–sulfur cluster on the Ni (100) surface aggregated to the heterojunction interface, forming a highly active electron-rich Fe–Ni 'electro-bridge' catalytic site, which should be one of the key origins of efficient electrochemical reduction of CO_2-to-CH_4. The calculation results can well correlate with the nickel-based and FeS-based catalytic materials reported in the recent experiments.[41–45] This bio-inspired design of the Ni100–Fe_4S_4 catalyst well combines the biological advantages of natural enzymes with the concepts of modern catalytic science, opening an avenue for the rational development of efficient artificial carbon fixation catalysts.

2. Computational details

All spin-polarized DFT calculations for periodic material systems were performed with the Vienna *Ab initio* simulation package (VASP)[46,47] using the projector-augmented wave (PAW) method.[48] The exchange–correlation function was handled using the generalized gradient approximation (GGA) formulated by the Revised Perdew–Burke–Ernzerhof (RPBE).[49] The van der Waals (vdW) interactions are described using the DFT-D3 method in Grimme's scheme.[50,51] The interaction between the atomic core and electrons was described by the projector augmented wave method. The plane-wave basis set energy cutoff was set to 500 eV. The Brillouin zone was sampled with a $2 \times 3 \times 1$ grid centered at the gamma (Γ) point for geometry relaxation. The perfect Ni bulk was fully optimized using $16 \times 16 \times 16$ *k*-point Gamma (Γ) centered Monkhorst–Pack mesh sampling. The Ni (100) facets were modeled using a four-layer 4×3 slab containing 96 atoms with 13.91 Å × 10.43 Å in *x* and *y* directions, respectively, and a 15 Å vacuum region, ensuring the negligible lateral interaction of the adsorbates. The Fe_4S_4 cluster absorbs on the Ni (100) surface, with 13.91 Å × 10.43 Å × 20.22 Å simulation boxes containing 107 atoms, the bottom two layers were kept frozen at the lattice position. All structural models with a dynamic magnetic moment were fully relaxed to optimize without any restrictions until their total energy gradient converged to $<1 \times 10^{-5}$ eV, and the average residual forces were <0.02 eV Å^{-1}. Moreover, the Gibbs free energy calculation is performed with the computational hydrogen electrode (CHE) model,[52] and the solvent effect is considered with the implicit solvent model implemented in VASPsol.[53,54] Position-specific charge values are obtained using Bader analysis.

3. Results and discussion

3.1 Designing catalysts by learning from nature

Nature provides a blueprint to efficiently activate CO_2 molecules and selectively generate useful fuels and value-added chemical feedstocks using metalloenzymes. To accelerate high-performance CO_2RR catalyst discovery, we propose a

method for the rational design of catalysts assisted by 'nature blueprints'. In this study, a dehydrogenase separated from *Carboxyothermus hydrogenoformans* (a bacterium isolated from a Russian hotspring[55]) was used as a 'nature blueprint' to aid in the structural design of Ni100–Fe_4S_4 (Fig. 1). CO dehydrogenases (CODHases) are the biological catalysts for the reversible oxidation of CO_2 to CO:[39]

$$CO_2(g) + 2H^+ + 2e^- \overset{\text{COD Hases}}{\longleftrightarrow} CO(g) + H_2O(l) \quad (1)$$

Fig. 1a shows the crystal structure of CO dehydrogenase II, which contains a special asymmetric [Ni-4Fe-5S] cluster. In the detailed crystal structure experimental data,[39,56] the structure of $CODHII_{Ch}$ with CO_2 reveals a triatomic ligand bridging Fe and Ni (Fig. 1b and c). This Fe–Ni bimetallic factor often plays a synergistic role in the catalytic reaction,[8,57] which is beneficial for the activation and catalytic conversion of CO_2. Based on this special asymmetric [Ni–4Fe–5S] cluster enzymatic active center, we designed a heterogeneous catalyst by loading Fe_4S_4 single-clusters on the Ni surface. The calculation results show that the adsorption energies (the equation is given in ESI S1†) of the Fe_4S_4 cluster on the three most common surfaces of nickel[58–62] Ni (100), Ni (111) and Ni (110) are −8.05 eV, −7.02 eV and −5.72 eV, respectively (Fig. S1†), indicating that the Fe_4S_4 cluster tends to adsorb on Ni (100) to form the most stable supported catalysts Ni100–Fe_4S_4. In addition, the Fe–O bonds (2.04 Å) and Ni–C bonds (1.99 Å) formed after the Ni100–Fe_4S_4 catalyst adsorbs CO_2 are only 0.01 Å and 0.03 Å different from those experimentally measured in $CODHII_{Ch}$ (Fe–O 2.05 Å, Ni–C 1.96 Å), respectively (Fig. 1c and d). The similar adsorption bond length means that Ni100–Fe_4S_4 and $CODHII_{Ch}$ have the same CO_2 binding mode, indicating that the Ni100–Fe_4S_4 catalyst may have enzyme-like catalytic activity.

3.2 Activating CO_2 beyond nature

The electroreduction of carbon dioxide by the catalyst is preferentially determined by the ability and degree of CO_2 activation. To activate CO_2 molecules, the active site basically needs to have the ability to adsorb CO_2. Since gaseous CO_2 molecules exhibit a linear shape and have stable triple-center π bonds (Fig. 2), ordinary physical adsorption hardly changes their geometric and electronic structures. Therefore, the activation of CO_2 molecules requires stronger chemisorption, and most forms of chemisorption will change the bond length and bond angle of CO_2 molecules, resulting in the splitting of its three-

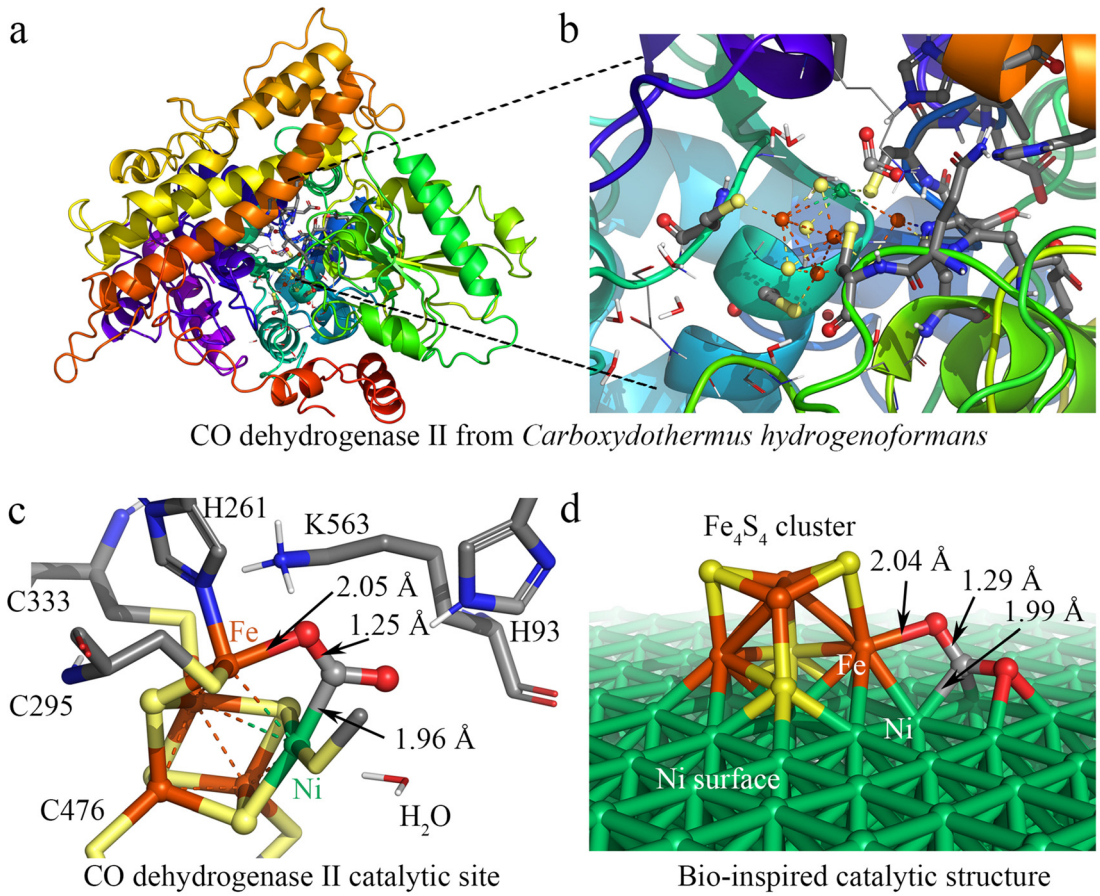

Fig. 1 Design of the Ni100–Fe_4S_4 catalyst inspired by CO dehydrogenase II. (a) The crystal structure of $CODHII_{Ch}$. (b) The catalytic center of $CODHII_{Ch}$. (c) The structure of the $CODHII_{Ch}$ catalytic center combined with CO_2. (d) The structure of the bio-inspired heterogeneous Ni100–Fe_4S_4 catalyst. (In atomic coloring, white is H, gray is C, blue is N, red is O, yellow is S, orange is Fe, and green is Ni).

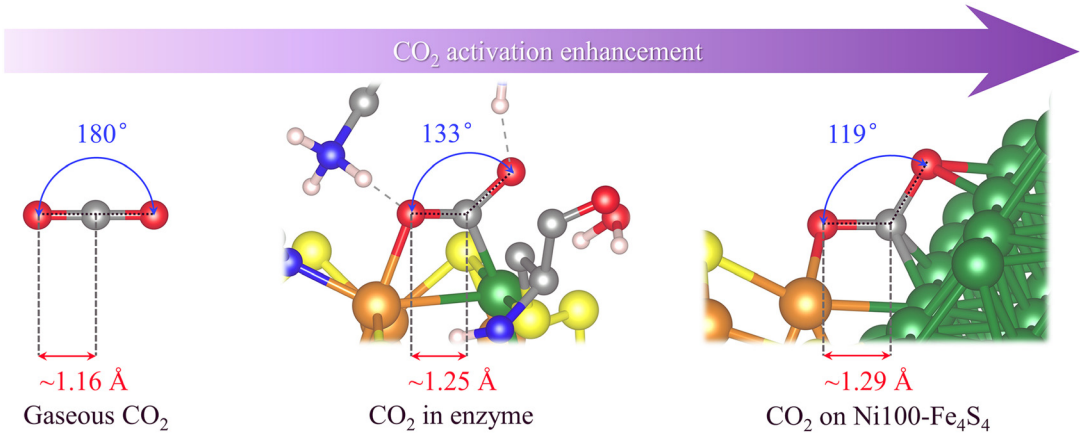

Fig. 2 Schematic diagram of the geometric structure of CO_2 in different adsorption states and CO_2 activation enhancement. (In atomic coloring, white is H, gray is C, blue is N, red is O, yellow is S, orange is Fe, and green is Ni).

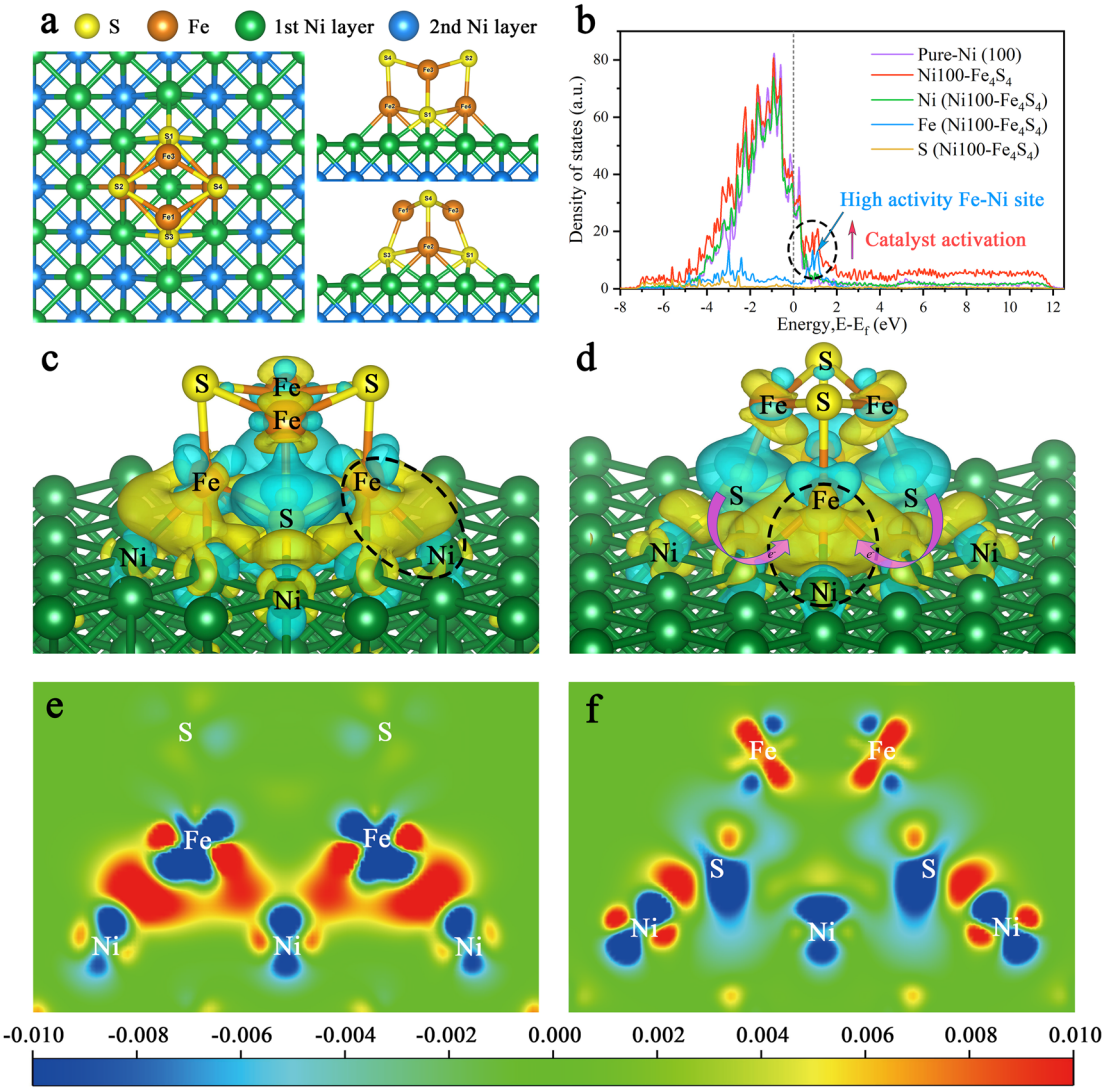

Fig. 3 The geometric and electronic structures of Ni100–Fe_4S_4. (a) The geometric structure of Ni100–Fe_4S_4. (b) The projected density of states (PDOS) onto the p and d states of Ni100–Fe_4S_4. (c and d) The charge difference analysis of the Ni100–Fe_4S_4 catalyst. (Light blue and yellow stand for the outflow and inflow of electrons, respectively. The black dotted circle represents the Fe–Ni site 'electro-bridge'. Magenta arrows represent electron flow from S to Fe–Ni sites.) (e and f) The tangent plane of charge difference in the Ni100–Fe_4S_4 catalyst. (Blue stands for the outflow and red for the inflow of electrons.).

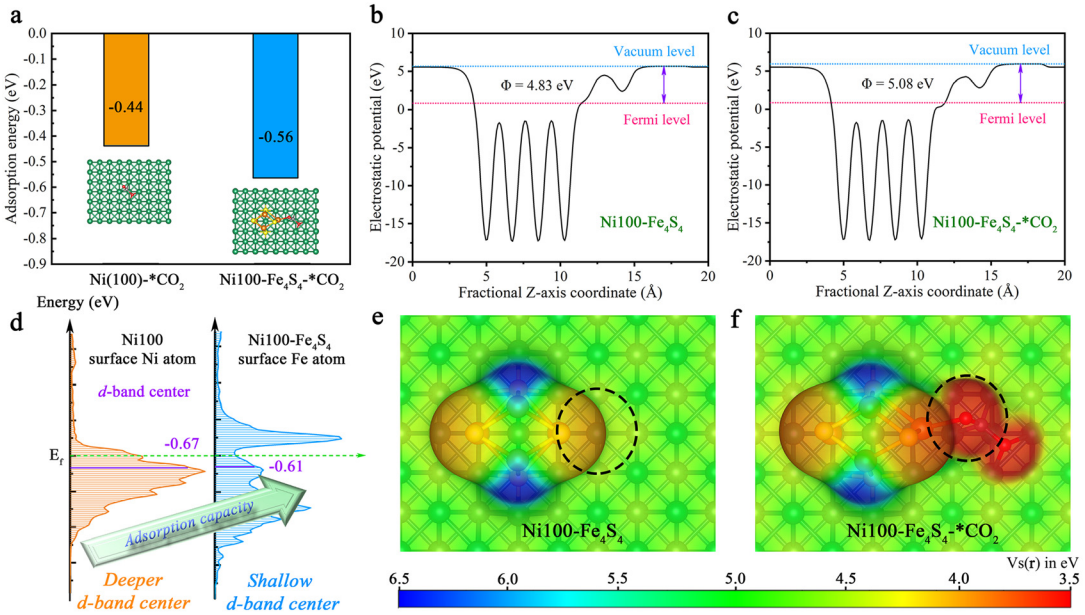

Fig. 4 The adsorption energy, d-band center, surface electrostatic potential and work function analysis of CO_2 adsorption. (a) Comparison of the adsorption energies between Ni (100) and Ni100–Fe_4S_4. (b) The work function of Ni100–Fe_4S_4. (c) The work function of Ni100–Fe_4S_4–*CO_2. (d) Comparison of the d-band centers between the Ni atom on Ni (100) and the Fe atom on Ni100–Fe_4S_4. (e) Electron-density isosurface of Ni100–Fe_4S_4. (f) Electron-density isosurface of Ni100–Fe_4S_4*–CO_2. The color bar stands for the scale of the electrostatic potential and the isosurfaces are plotted at the 0.002 e bohr^{-3} level.

center π bond. The geometric and electronic structures are subsequently changed, exhibiting a metastable activated CO_2 molecule.

As shown in Fig. 2, the crystal structure obtained by rotating anode X-ray diffraction[39] shows that the CO_2 molecules adsorbed on the catalytically active site of $CODHII_{Ch}$ are no longer linear in gaseous CO_2. Its ∠O–C–O angle is 133°, and the C–O bond length elongates from 1.16 Å to 1.25 Å compared with gaseous CO_2 molecules. Interestingly, in the structure of Ni100–Fe_4S_4 adsorbing CO_2, its ∠O–C–O angle is smaller than that in $CODHII_{Ch}$, only 119°, and the C–O bond is also longer, reaching 1.29 Å. A smaller ∠O–C–O angle and longer C–O bonds indicate that the designed Ni100–Fe_4S_4, inspired by the active center structure of $CODHII_{Ch}$, exhibits stronger CO_2 activation ability.

3.3 Fe–Ni 'electro-bridge' enhanced CO_2 activation

Bio-inspired strategies to control the performance of CO_2 activation focus on the geometric and electronic structures of the active site. We applied this methodology to the design of Ni100–Fe_4S_4. Fig. 3a shows the top view, front view and side view of the Ni100–Fe_4S_4 catalyst structure, which was obtained by loading Fe_4S_4 iron–sulfur clusters onto the Ni (100) surface. The geometric structure is the global energy minimum obtained by spin-polarized first-principles calculations. These iron–sulfur clusters, which are commonly used in biology to transfer electrons, are stabilized on the Ni (100) surface to form a special Ni100–Fe_4S_4 cluster heterojunction interface structure.

To unveil the origin of the structural activity of the Ni100–Fe_4S_4 heterojunction, we further calculated the projected density of states (PDOS) onto the p and d states of Ni100–Fe_4S_4 (Fig. 3b). In the PDOS of Ni100–Fe_4S_4, the peak near the Fermi level is mainly composed of Fe and Ni, implying that Fe–Ni is a highly active site. The Fe–Ni site in Ni100–Fe_4S_4 mimics the Fe–Ni catalytic sites in $CODHII_{Ch}$, which are crucial for CO_2 activation and reaction selectivity. Owing to the interaction of the heterojunction interface between Ni (100) and Fe_4S_4, the surface Ni atoms and Fe_4S_4 iron–sulfur clusters could transfer charge to the Fe–Ni site and an optimized polarization field is generated on its surface.

Furthermore, charge difference analysis results show that a large number of electrons are transferred from the Fe_4S_4 iron–sulfur clusters and the Ni (100) surface to the Fe–Ni site, forming a highly active electron-rich Fe–Ni 'electro-bridge' catalytic site on the heterojunction interface (Fig. 3c–f). Here, the role of S atoms is also very important. Through the charge difference calculation, we can observe that most of the charges on the Fe–Ni site come from S (Fig. 3d, magenta arrow), and the S atom acts as the charge supplier of the active site of the catalyst. Therefore, the Fe–Ni site can inject enough electrons into the CO_2 2π* antibonding orbitals, disrupting the strong sp-hybridization symmetry of the carbon atom.

3.4 The mechanism of CO_2 adsorption and activation

Based on the above designed structure by bio-inspired strategies, the adsorption models for theoretical calculations can be constructed to gain insights into the CO_2 adsorption step

on Ni100–Fe_4S_4 from an atomic/electronic-level standpoint. Specifically, the thermodynamic energy conversion, d-band center, work function and electron-density isosurfaces were used to theoretically and systematically reveal the mechanism of the CO_2 adsorption step on Ni100–Fe_4S_4. To shed light on the characteristics and performance of Ni100–Fe_4S_4 adsorption of CO_2, we first analyzed the adsorption energy (the equation is ESI S2†). As depicted in Fig. 4a, Ni100–Fe_4S_4 shows a much more significant thermodynamic energy conversion of the CO_2 adsorption step (−0.56 eV) than pure Ni (100) (−0.44 eV). Pure Ni (100) has been widely proven to be a good CO_2 adsorbent both theoretically and experimentally.[41,63–65] This means Ni100–Fe_4S_4 tends to well adsorb CO_2 in theory, which is well in line with the d-band center (Fig. 4d, the equation is ESI S3†). The favorable adsorption of CO_2 on Ni100–Fe_4S_4 will accelerate its CO_2RR processes and promote its CO_2RR activity.

To investigate the electronic structure and surface adsorption behavior on Ni100–Fe_4S_4, we calculated the electron-density isosurface (Fig. 4b and c) and the electronic work function (Fig. 4e and f) for Ni100–Fe_4S_4 and Ni100–Fe_4S_4–*CO_2, respectively. The work function is an essential physical property of metallic materials,[66] which has been widely used in the design and evaluation of various photo/electrocatalysts,[67–69] can be obtained by calculating the difference between the electrostatic potential at the vacuum level E_{vac} and the electrostatic potential at the Fermi level E_F using ESI eqn (S4) and (S5).† The detailed electrostatic potential and work function calculation formula are given in ESI S3 and S4.† As shown in Fig. 4b and c, the work function of Ni100–Fe_4S_4 increases from

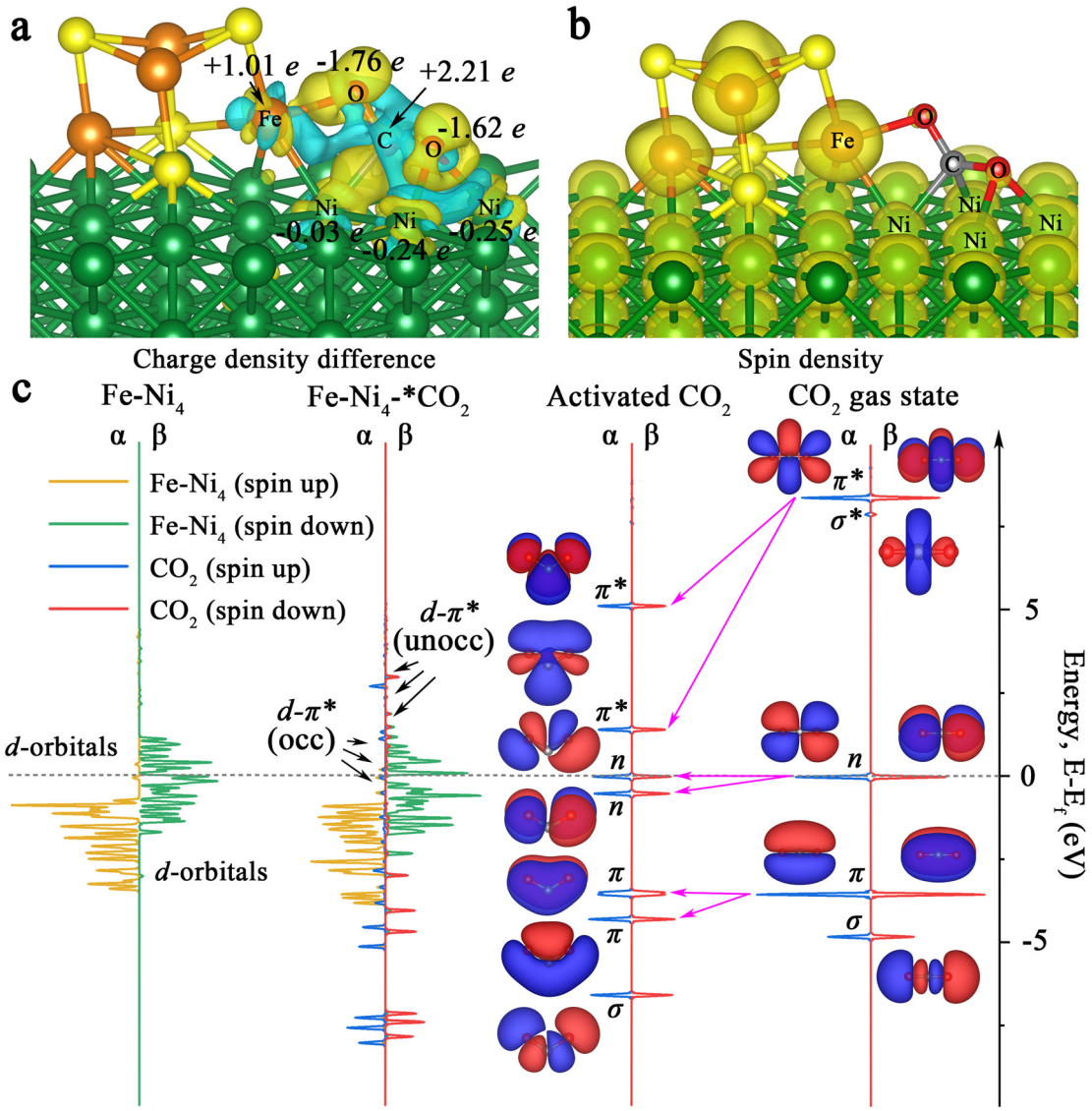

Fig. 5 Associative and activation mechanism analysis. (a) Charge density difference of CO_2 adsorption on Ni100–Fe_4S_4 (Light blue stands for the outflow and yellow for the inflow of electrons.). (b) Spin density of Ni100–Fe_4S_4 (Yellow stands for spin electrons.). (c) Projected electronic densities of states (PDOS) of $FeNi_4$, CO_2 and their interactive configuration $FeNi_4$–*CO_2.

4.83 eV to 5.08 eV after CO_2 adsorption, which means that the electrons on the surface of Ni100–Fe_4S_4 flow to the CO_2 molecule, thereby increasing the work function of the system. According to previous reports, the surface energy of the system is inversely proportional to the work function.[70] Therefore, the adsorption step of CO_2 on Ni100–Fe_4S_4 simultaneously reduces the surface energy of the system and increases the stability of the material surface. Meanwhile, the electron-density isosurface demonstrates that the Fe–Ni sites with a lower electrostatic potential (Fig. 4e, black dotted circle area) on the Ni100–Fe_4S_4 surface are favorable for the nucleophilic attack on the electrophilic carbonyl carbon of CO_2 molecules. In addition, the electrostatic potentials around the isosurface of the O atom of CO_2 are at a low level (Fig. 4f, black dotted circle area), indicating a selective hydrogenation site.

Also, we calculated the charge distribution of Ni100–Fe_4S_4–*CO_2. As presented in Fig. 5a, we can clearly observe the electron inflow into the two O atoms of the adsorbed CO_2 in Ni100–Fe_4S_4–*CO_2 by the charge density difference. Further Bader charge analysis showed that electrons flowed mainly

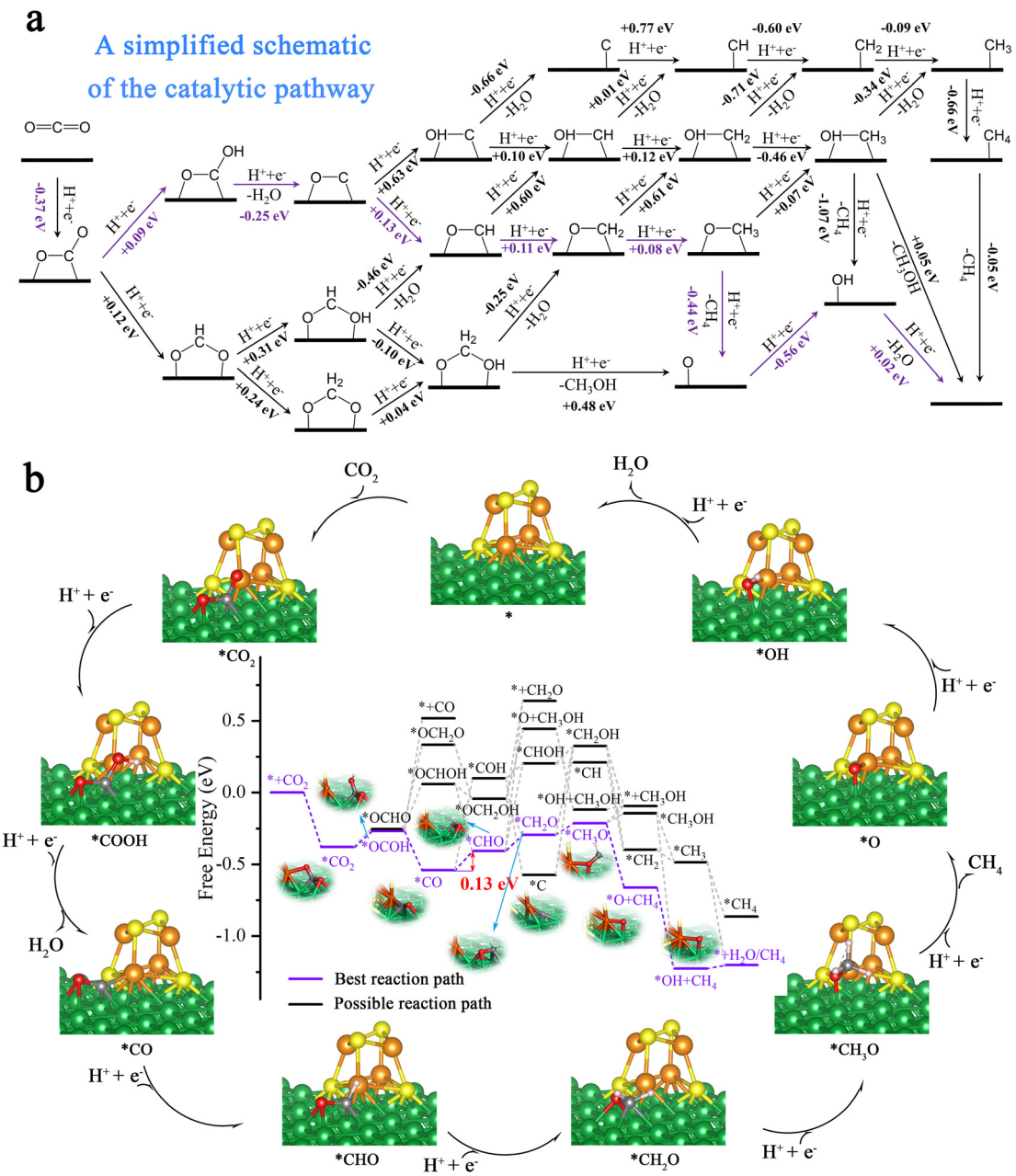

Fig. 6 The CO_2RR pathways on Ni100–Fe_4S_4. (a) A simplified schematic of the free energy changes (ΔG) in the entire possible CO_2RR pathways; the energy optimal route is marked in purple. (b) The schematic diagram of the reaction mechanism of CO_2 electroreduction to CH_4 during the entire CO_2 reduction catalytic cycles.

from Fe atoms to CO_2 molecules attributed to the large spin polarization on Fe (Fig. 5b), which is consistent with the electron-density isosurface and work function analysis. Remarkably, in this charge transfer mode, the C atom of the CO_2 molecule has a highly positive charge (+2.21*e*), and the oxygen atoms have highly negative charges (−1.76*e* and −1.62*e*), which means that the most negatively charged oxygen atomic site (−1.76*e*) is more favorable for the subsequent electrocatalytic step to combine with H^+. This selectivity of the hydrogenation site is consistent with subsequent Gibbs free energy calculations (Fig. 6, ESI Tables S1 and S4†).

To elucidate the bonding nature of the CO_2 molecules and Ni100–Fe_4S_4 involved in the associative mechanism, we further calculated the densities of states (DOS) of Ni100–Fe_4S_4–*CO_2 and Fe–Ni_4 sites (five atoms in Ni100–Fe_4S_4 directly affected by CO_2 molecules) for comparison (Fig. 5c). By comparing the DOS and molecular orbitals of the gaseous linear CO_2 molecule and the activated bent CO_2 molecule, we found that the π, n and π* orbitals of the CO_2 molecule were split after activation. The π* orbital splits into two empty orbitals with unequal energy levels in the activated CO_2 molecule, which matched well with the Fe–Ni_4 polarized β-spin d orbitals near the Fermi level, forming partially occupied d–π* hybrid orbitals. Although the energy levels of the majority α-spin d orbitals of Fe–Ni_4 are about 2.0 eV lower than the π* orbitals of activated CO_2, the results show that the interaction between the α orbitals and the π* orbitals is obvious. This α-orbital interaction is due to the fact that there are still minority α orbitals present near the Fermi level, matching the π* orbitals of the CO_2 molecule. This CO_2 activation mechanism reveals that the electrons from the d orbitals of Ni100–Fe_4S_4 partially transfer to the empty π* orbitals of adsorbed CO_2, which is consistent with the charge density difference analysis (Fig. 5a) and DOS analysis (Fig. 5c).

3.5 Reaction mechanism of CO_2 electroreduction to CH_4

In order to further evaluate the activity and selectivity of Ni100–Fe_4S_4 to convert CO_2* to hydrocarbon species, we studied the free energy changes (ΔG) of the entire CO_2 reduction catalytic cycles. We first considered the adsorption pattern of CO_2 molecules on the Ni100–Fe_4S_4 surface (ESI Fig. S2, Table S4†), DFT calculations showed that CO_2 molecules tended to be in the C–O site adsorption pattern (ESI Fig. S2c†) rather than the O–O site (ESI Fig. S2a†) adsorption pattern. This adsorption pattern is consistent with previously reported Ni-based materials.[63,64] Then, the free energy calculation results (Fig. 6a) confirmed that the first hydrogenation step of the CO_2RR is preferentially on O to form COOH* rather than C (OCHO*) due to the low level of electrostatic potentials around the isosurface of the O atom of CO_2 (Fig. 4f, black dotted circle area, ESI Table S4†). During the entire hydrogenation steps and reduction mechanism of CO_2, the CO_2RR on Ni100–Fe_4S_4 follows the circulation pathway of * → CO_2* → COOH* → CO* → CHO* → CH_2O* → CH_3O* → O* → OH* → H_2O* → *, with the final products of CH_4 and H_2O (Fig. 6b). With this Ni100–Fe_4S_4 catalyst, the potential determining step (PDS) is CO* → CHO*, and the entire catalytic cycle has a limiting potential of only 0.13 eV, which is much lower than those

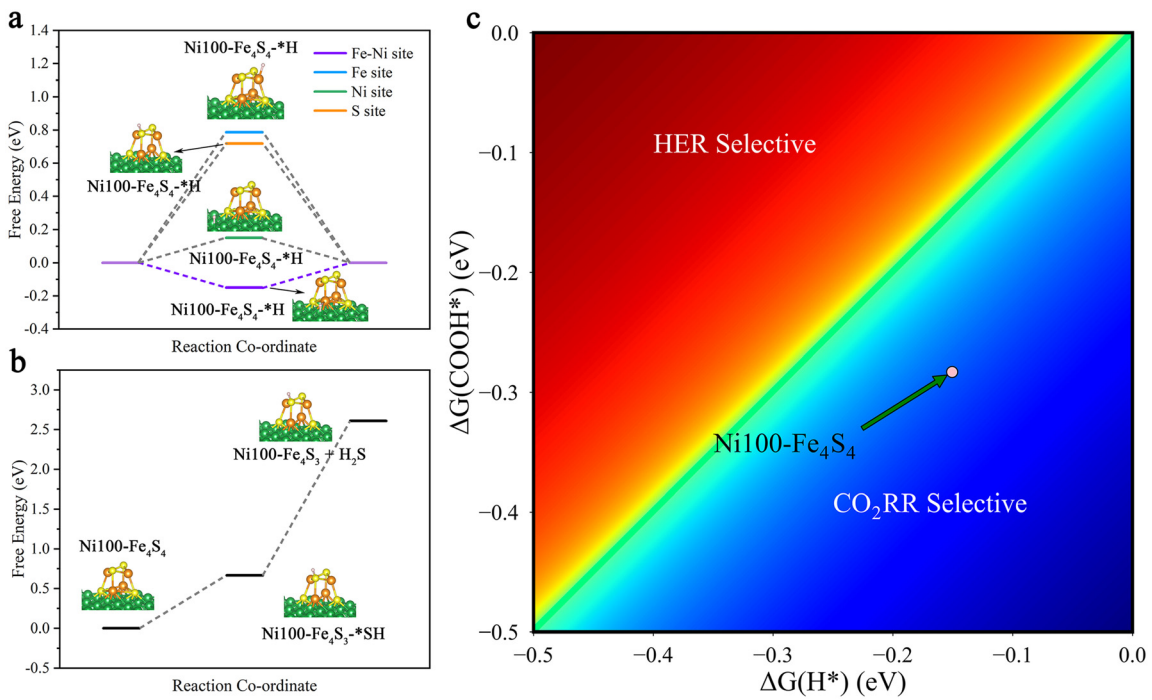

Fig. 7 Selectivity between the CO_2RR, the HER and the H_2SER. (a) Free energy diagrams of the possible HER mechanisms on the Fe–Ni, Fe, Ni and S sites. (b) Free energy diagrams of the possible H_2SER mechanisms on the cluster. (c) Selectivity for the CO_2RR *vs.* HER; the light pink data points represent the Ni100–Fe_4S_4 catalyst, and the blue region represents higher selectivity to the CO_2RR, while the red region to the HER.

of most reported CO_2RR catalysts in recent years (ESI Table S2†). Therefore, Ni100–Fe_4S_4 is potentially an efficient CO_2RR catalyst producing CH_4 at a low overpotential selectively.

3.6 Selectivity for CO_2 electroreduction

In order to study the stability of the cluster and the selectivity of the catalyst, we considered side reactions involving the hydrogen evolution reaction (HER) and the H_2S evolution reaction (H_2SER). The HER is an important competing side reaction, which can constantly consume proton–electron pairs from the electrolyte solution, restraining the faradaic efficiency of the CO_2RR significantly.[14,71,72] To identify possible HER side-reaction sites, we first calculated Gibbs free energy changes (ΔG) of the HER ($* + H^+ + e^- \rightarrow H^*$) on the Fe–Ni, Fe, Ni and S sites (Fig. 7a, ESI Table S4†). According to the Brønsted–Evans–Polanyi relation,[73,74] the result shows that the Fe–Ni site with a lower $\Delta G = -0.15$ eV is kinetically more favored due to the smaller reaction barriers. Besides, the calculated results show that hydrogenation is preferentially on O to form COOH* rather than C (OCHO*) both thermodynamically and kinetically (ESI Table S4,† Fig. 4). So, we compare the HER with the first hydrogenation step of the CO_2RR ($* + CO_2(g) + H^+ + e^- \rightarrow$ COOH*). The heatmap diagram of the Gibbs free energy changes (Fig. 7c) indicates that Ni100–Fe_4S_4 has higher selectivity toward the CO_2RR.

The H_2S evolution reaction is a possible dissociation event on Fe_4S_4 clusters.[75] To test the stability of Ni100–Fe_4S_4, we calculated and plotted the free energy of the H_2SER in Fig. 7b and ESI Table S4.† The calculated thermodynamic energy barrier is quite large $\Delta G = +1.94$ eV, which suggests that the H_2SER on Ni100–Fe_4S_4 is thermodynamically difficult and the reduction of Fe_4S_4 to Fe in metallic form is more difficult. Therefore, the analysis results of side reactions demonstrate that the Ni100–Fe_4S_4 catalyst is promising as a cathode material for the CO_2RR with high selectivity and faradaic efficiency.

4. Conclusion

In conclusion, we propose a strategy for the bio-inspired design approach of CO_2RR catalysts at the atomic level. Taking Ni100–Fe_4S_4 as an example, we designed this heterogeneous single-cluster catalyst by imitating the spatial structure of the Fe–Ni active center in CO dehydrogenase II from *Carboxyothermus hydrogenoformans*. We found that Ni100–Fe_4S_4 exhibits a stronger CO_2 activation ability than natural CO dehydrogenase by analyzing the changes in the CO_2 adsorption state, geometric structure and electronic structure. This excellent CO_2 activation ability of Ni100–Fe_4S_4 is mainly attributed to the Fe–Ni site designed by the bio-inspired strategy, forming a Fe–Ni 'electro-bridge' enhanced CO_2 activation. The detailed electronic structure analysis shows that the electrons from the Fe–Ni site's d orbitals partially transfer to the empty π^* orbitals of CO_2, leading to partial occupation of the formed d–π^* orbitals. Moreover, the free energy changes (ΔG) of the entire CO_2 reduction catalytic cycles were calculated. A detailed study on the reaction mechanism of CO_2 electroreduction shows that CO_2RR on Ni100–Fe_4S_4 follows the circulation pathway of $* \rightarrow CO_2^* \rightarrow COOH^* \rightarrow CO^* \rightarrow CHO^* \rightarrow CH_2O^* \rightarrow CH_3O^* \rightarrow O^* \rightarrow OH^* \rightarrow H_2O^* \rightarrow *$, with the final products of CH_4 and H_2O. To be more rigorous, the side reactions involving the hydrogen evolution reaction (HER) and the H_2S evolution reaction (H_2SER) were also performed and proved to be thermodynamically unfavorable. These promising results show the feasibility of using a Ni100–Fe_4S_4 catalyst as the cathode for the CO_2RR with high selectivity and faradaic efficiency. Therefore, bio-inspired strategies as a transformative approach can be directly applied to heterogeneous catalysts. The clever use of these bio-inspired strategies in modern catalyst design will lead our catalysts beyond their current limitations exploring the final frontier of catalysis.

Author contributions

Hengyue Xu: conceptualization, data curation, formal analysis, investigation, methodology, and writing – original draft. Daqin Guan: formal analysis and writing – review & editing. Lan Ma: project administration, resources, and supervision.

Conflicts of interest

The authors declare no competing interests.

Acknowledgements

This research was funded by the Institute of Biomedical Health Technology and Engineering, Shenzhen Bay Laboratory. We are grateful to the Shenzhen Bay Laboratory Supercomputing Center for providing the high performance computing platform.

References

1 P. M. Cox, R. A. Betts, C. D. Jones, S. A. Spall and I. J. Totterdell, *Nature*, 2000, **408**, 184–187.
2 V. Humphrey, J. Zscheischler, P. Ciais, L. Gudmundsson, S. Sitch and S. I. Seneviratne, *Nature*, 2018, **560**, 628–631.
3 I. P. Montañez, N. J. Tabor, D. Niemeier, W. A. DiMichele, T. D. Frank, C. R. Fielding, J. L. Isbell, L. P. Birgenheier and M. C. Rygel, *Science*, 2007, **315**, 87–91.
4 C. D. Thomas, A. Cameron, R. E. Green, M. Bakkenes, L. J. Beaumont, Y. C. Collingham, B. F. Erasmus, M. F. De Siqueira, A. Grainger and L. Hannah, *Nature*, 2004, **427**, 145–148.
5 Z. W. Seh, J. Kibsgaard, C. F. Dickens, I. Chorkendorff, J. K. Norskov and T. F. Jaramillo, *Science*, 2017, **355**, 1.

6 Y. Y. Birdja, E. Pérez-Gallent, M. C. Figueiredo, A. J. Göttle, F. Calle-Vallejo and M. T. M. Koper, *Nat. Energy*, 2019, **4**, 732–745.
7 J. D. Benck, T. R. Hellstern, J. Kibsgaard, P. Chakthranont and T. F. Jaramillo, *ACS Catal.*, 2014, **4**, 3957–3971.
8 J. Li, H. Huang, W. Xue, K. Sun, X. Song, C. Wu, L. Nie, Y. Li, C. Liu, Y. Pan, H.-L. Jiang, D. Mei and C. Zhong, *Nat. Catal.*, 2021, **4**, 719–729.
9 X. Zhang, Y. Wang, M. Gu, M. Wang, Z. Zhang, W. Pan, Z. Jiang, H. Zheng, M. Lucero, H. Wang, G. E. Sterbinsky, Q. Ma, Y.-G. Wang, Z. Feng, J. Li, H. Dai and Y. Liang, *Nat. Energy*, 2020, **5**, 684–692.
10 Z. L. Wang, J. Choi, M. Xu, X. Hao, H. Zhang, Z. Jiang, M. Zuo, J. Kim, W. Zhou, X. Meng, Q. Yu, Z. Sun, S. Wei, J. Ye, G. G. Wallace, D. L. Officer and Y. Yamauchi, *ChemSusChem*, 2020, **13**, 929–937.
11 Z. Zhang, L. Bian, H. Tian, Y. Liu, Y. Bando, Y. Yamauchi and Z. L. Wang, *Small*, 2022, **18**, 2107450.
12 Z. X. Cai, Z. L. Wang, Y. J. Xia, H. Lim, W. Zhou, A. Taniguchi, M. Ohtani, K. Kobiro, T. Fujita and Y. Yamauchi, *Angew. Chem., Int. Ed.*, 2021, **60**, 4747–4755.
13 K. Tran and Z. W. Ulissi, *Nat. Catal.*, 2018, **1**, 696–703.
14 M. Zhong, K. Tran, Y. Min, C. Wang, Z. Wang, C.-T. Dinh, P. De Luna, Z. Yu, A. S. Rasouli, P. Brodersen, S. Sun, O. Voznyy, C.-S. Tan, M. Askerka, F. Che, M. Liu, A. Seifitokaldani, Y. Pang, S.-C. Lo, A. Ip, Z. Ulissi and E. H. Sargent, *Nature*, 2020, **581**, 178–183.
15 H. S. Shafaat and J. Y. Yang, *Nat. Catal.*, 2021, **4**, 928–933.
16 H.-B. Wang, J.-Q. Wang, R. Zhang, C.-Q. Cheng, K.-W. Qiu, Y.-j. Yang, J. Mao, H. Liu, M. Du, C.-K. Dong and X.-W. Du, *ACS Catal.*, 2020, **10**, 4914–4921.
17 H. Zhang, L. Huang, J. Chen, L. Liu, X. Zhu, W. Wu and S. Dong, *Nano Energy*, 2021, **83**, 105798.
18 P. T. Cesana, B. X. Li, S. G. Shepard, S. I. Ting, S. M. Hart, C. M. Olson, J. I. Martinez Alvarado, M. Son, T. J. Steiman, F. N. Castellano, A. G. Doyle, D. W. C. MacMillan and G. S. Schlau-Cohen, *Chem*, 2022, **8**, 174–185.
19 C. Ren, P. Yang, J. Sun, E. Y. Bi, J. Gao, J. Palmer, M. Zhu, Y. Wu and J. Liu, *J. Am. Chem. Soc.*, 2021, **143**, 7891–7896.
20 N. S. Weliwatte and S. D. Minteer, *Joule*, 2021, **5**, 2564–2592.
21 R. Braakman and E. Smith, *PLoS Comput. Biol.*, 2012, **8**, e1002455.
22 I. A. Berg, D. Kockelkorn, W. H. Ramos-Vera, R. F. Say, J. Zarzycki, M. Hugler, B. E. Alber and G. Fuchs, *Nat. Rev. Microbiol.*, 2010, **8**, 447–460.
23 M. Calvin and A. A. Benson, *Science*, 1948, **107**, 476–480.
24 M. Evans, B. B. Buchanan and D. I. Arnon, *Proc. Natl. Acad. Sci. U. S. A.*, 1966, **55**, 928.
25 M. Schulman, D. Parker, L. G. Ljungdahl and H. G. Wood, *J. Bacteriol.*, 1972, **109**, 633–644.
26 G. Strauss and G. Fuchs, *Eur. J. Biochem.*, 1993, **215**, 633–643.
27 I. A. Berg, D. Kockelkorn, W. Buckel and G. Fuchs, *Science*, 2007, **318**, 1782–1786.
28 H. Huber, M. Gallenberger, U. Jahn, E. Eylert, I. A. Berg, D. Kockelkorn, W. Eisenreich and G. Fuchs, *Proc. Natl. Acad. Sci. U. S. A.*, 2008, **105**, 7851–7856.
29 T. Schwander, L. S. v. Borzyskowski, S. Burgener, N. S. Cortina and T. J. Erb, *Science*, 2016, **354**, 900–904.
30 S. J. Varma, K. B. Muchowska, P. Chatelain and J. Moran, *Nat. Ecol. Evol.*, 2018, **2**, 1019–1024.
31 M. Can, F. A. Armstrong and S. W. Ragsdale, *Chem. Rev.*, 2014, **114**, 4149–4174.
32 C. L. Drennan, T. I. Doukov and S. W. Ragsdale, *J. Biol. Inorg. Chem.*, 2004, **9**, 511–515.
33 P. S. Adam, G. Borrel and S. Gribaldo, *Proc. Natl. Acad. Sci. U. S. A.*, 2018, **115**, E1166–E1173.
34 D. C. Catling and K. J. Zahnle, *Sci. Adv.*, 2020, **6**, eaax1420.
35 G. P. Glasby, *Episodes*, 1998, **21**, 252–256.
36 J. Ruickoldt, Y. Basak, L. Domnik, J.-H. Jeoung and H. Dobbek, *ACS Catal.*, 2022, **12**, 13131–13142.
37 J. Fesseler, J.-H. Jeoung and H. Dobbek, *Angew. Chem., Int. Ed.*, 2015, **54**, 8560–8564.
38 D.-H. Nam, P. De Luna, A. Rosas-Hernández, A. Thevenon, F. Li, T. Agapie, J. C. Peters, O. Shekhah, M. Eddaoudi and E. H. Sargent, *Nat. Mater.*, 2020, **19**, 266–276.
39 J.-H. Jeoung and H. Dobbek, *Science*, 2007, **318**, 1461–1464.
40 P. J. Ogren, *J. Chem. Educ.*, 2002, **79**, 117.
41 W. Gac, W. Zawadzki, M. Rotko, M. Greluk, G. Słowik and G. Kolb, *Catal. Today*, 2020, **357**, 468–482.
42 M.-A. Serrer, A. Gaur, J. Jelic, S. Weber, C. Fritsch, A. H. Clark, E. Saraçi, F. Studt and J.-D. Grunwaldt, *Catal. Sci. Technol.*, 2020, **10**, 7542–7554.
43 T. A. Le, M. S. Kim, S. H. Lee, T. W. Kim and E. D. Park, *Catal. Today*, 2017, **293–294**, 89–96.
44 Y. Gao, L. Dou, S. Zhang, L. Zong, J. Pan, X. Hu, H. Sun, K. K. Ostrikov and T. Shao, *Chem. Eng. J.*, 2021, **420**, 127693.
45 T. G. Senthamaraikannan and D.-H. Lim, *J. Phys. Chem. C*, 2022, **126**, 7012–7021.
46 G. Kresse and J. Furthmüller, *Comput. Mater. Sci.*, 1996, **6**, 15–50.
47 G. Kresse and J. Furthmüller, *Phys. Rev. B: Condens. Matter Mater. Phys.*, 1996, **54**, 11169.
48 P. E. Blöchl, *Phys. Rev. B: Condens. Matter Mater. Phys.*, 1994, **50**, 17953.
49 B. Hammer, L. B. Hansen and J. K. Nørskov, *Phys. Rev. B: Condens. Matter Mater. Phys.*, 1999, **59**, 7413.
50 S. Grimme, *J. Comput. Chem.*, 2006, **27**, 1787–1799.
51 S. Grimme, J. Antony, S. Ehrlich and H. Krieg, *J. Chem. Phys.*, 2010, **132**, 154104.
52 J. K. Nørskov, J. Rossmeisl, A. Logadottir, L. Lindqvist, J. R. Kitchin, T. Bligaard and H. Jonsson, *J. Phys. Chem. B*, 2004, **108**, 17886–17892.
53 K. Mathew, R. Sundararaman, K. Letchworth-Weaver, T. Arias and R. G. Hennig, *J. Chem. Phys.*, 2014, **140**, 084106.
54 K. Mathew, V. C. Kolluru, S. Mula, S. N. Steinmann and R. G. Hennig, *J. Chem. Phys.*, 2019, **151**, 234101.
55 M. Wu, Q. Ren, A. S. Durkin, S. C. Daugherty, L. M. Brinkac, R. J. Dodson, R. Madupu, S. A. Sullivan,

J. F. Kolonay, W. C. Nelson, L. J. Tallon, K. M. Jones, L. E. Ulrich, J. M. Gonzalez, I. B. Zhulin, F. T. Robb and J. A. Eisen, *PLoS Genet.*, 2005, **1**, e65.
56 H. Dobbek, V. Svetlitchnyi, L. Gremer, R. Huber and O. Meyer, *Science*, 2001, **293**, 1281–1285.
57 Y. Wang, L. Cao, N. J. Libretto, X. Li, C. Li, Y. Wan, C. He, J. Lee, J. Gregg, H. Zong, D. Su, J. T. Miller, T. Mueller and C. Wang, *J. Am. Chem. Soc.*, 2019, **141**, 16635–16642.
58 N. Al-Sarraf, J. T. Stuckless and D. A. King, *Nature*, 1992, **360**, 243–245.
59 K. Y. Ma, L. Zhang, S. Jin, Y. Wang, S. I. Yoon, H. Hwang, J. Oh, D. S. Jeong, M. Wang, S. Chatterjee, G. Kim, A.-R. Jang, J. Yang, S. Ryu, H. Y. Jeong, R. S. Ruoff, M. Chhowalla, F. Ding and H. S. Shin, *Nature*, 2022, **606**, 88–93.
60 X. Ding, L. De Rogatis, E. Vesselli, A. Baraldi, G. Comelli, R. Rosei, L. Savio, L. Vattuone, M. Rocca, P. Fornasiero, F. Ancilotto, A. Baldereschi and M. Peressi, *Phys. Rev. B*, 2007, **76**, 195425.
61 T. Suzuki, T. Yamada and K. Itaya, *J. Phys. Chem.*, 1996, **100**, 8954–8961.
62 J. Stuckless, C. Wartnaby, N. Al-Sarraf, S. J. Dixon-Warren, M. Kovar and D. King, *J. Chem. Phys.*, 1997, **106**, 2012–2030.
63 J. Cai, Y. Han, S. Chen, E. J. Crumlin, B. Yang, Y. Li and Z. Liu, *J. Phys. Chem. C*, 2019, **123**, 12176–12182.
64 A. Farjamnia and B. Jackson, *J. Chem. Phys.*, 2017, **146**, 074704.
65 X. Zhou, B. Kolb, X. Luo, H. Guo and B. Jiang, *J. Phys. Chem. C*, 2017, **121**, 5594–5602.
66 N. D. Lang and W. Kohn, *Phys. Rev. B: Solid State*, 1971, **3**, 1215–1223.
67 D. Guan, J. Zhong, H. Xu, Y.-C. Huang, Z. Hu, B. Chen, Y. Zhang, M. Ni, X. Xu, W. Zhou and Z. Shao, *Appl. Phys. Rev.*, 2022, **9**, 011422.
68 H. Xu and D. Guan, *ACS Appl. Mater. Interfaces*, 2022, **14**, 51190–51199.
69 X. Guo, H. Xu, W. Li, Y. Liu, Y. Shi, Q. Li and H. Pang, *Adv. Sci.*, 2022, 2206084, DOI: **10.1002/advs.202206084**.
70 J. Wang and S.-q. Wang, *Appl. Surf. Sci.*, 2015, **357**, 1046–1052.
71 X. Hong, K. Chan, C. Tsai and J. K. Nørskov, *ACS Catal.*, 2016, **6**, 4428–4437.
72 L. Ju, X. Tan, X. Mao, Y. Gu, S. Smith, A. Du, Z. Chen, C. Chen and L. Kou, *Nat. Commun.*, 2021, **12**, 5128.
73 J. Bronsted, *Chem. Rev.*, 1928, **5**, 231–338.
74 M. Evans and M. Polanyi, *Trans. Faraday Soc.*, 1938, **34**, 11–24.
75 J. B. Varley, H. A. Hansen, N. L. Ammitzbøll, L. C. Grabow, A. A. Peterson, J. Rossmeisl and J. K. Nørskov, *ACS Catal.*, 2013, **3**, 2640–2643.